Ultracold-neutron production in a pulsed-neutron beam line

C. M. Lavelle, C.-Y. Liu,* W. Fox, G. Manus, P. M. McChesney, D. J. Salvat, and Y. Shin†
Physics Department, Indiana University, Bloomington, Indiana 47408, USA

M. Makela, C. Morris, and A. Saunders
Physics Division, P25, Los Alamos National Laboratory, Los Alamos, New Mexico 87544, USA

A. Couture
LANSCE Division, Nuclear Science, Los Alamos National Laboratory, Los Alamos, New Mexico 87544, USA

A. R. Young
Physics Department, North Carolina State University, Raleigh, North Carolina 27695, USA
(Received 15 April 2010; published 19 July 2010)

We present the results of an ultracold neutron (UCN) production experiment in a pulsed-neutron beam line at the Los Alamos Neutron Scattering Center. The experimental apparatus allows for a comprehensive set of measurements of UCN production as a function of target temperature, incident neutron energy, target volume, and applied magnetic field. However, the low counting statistics of the UCN signal can be overwhelmed by the large background associated with the scattering of the primary cold-neutron flux that is required for UCN production. We have developed a background subtraction technique that takes advantage of the very different time-of-flight profiles between the UCN and the cold neutrons, in the pulsed beam. Using the unique timing structure, we can reliably extract the UCN signal. Solid ortho-$^2H_2$ is used to calibrate UCN transmission through the apparatus, which is designed primarily for studies of UCN production in solid O_2. In addition to setting the overall detection efficiency in the apparatus, UCN production data using solid $^2H_2$ suggest that the UCN upscattering cross section is smaller than previous estimates, indicating the deficiency of the incoherent approximation widely used to estimate inelastic cross sections in the thermal and cold regimes.

DOI: 10.1103/PhysRevC.82.015502 PACS number(s): 29.25.Dz, 28.20.Gd

I. INTRODUCTION

Ultracold neutrons (UCNs) are free neutrons with maximum energies of 300 neV, equivalent to ∼1 mK. Their kinetic energy is so low that they may be contained and accumulated in material bottles, magnetic traps, and the Earth's gravitational field, for durations up to hundreds of seconds [1]. The kinetic energy is comparable to the Zeeman splitting in a magnetic field of a few tesla, and a neutron state with 100% spin polarization can be prepared through simple field filtering. The ability to be stored and easy polarization of UCNs make them the tool of choice in many experiments to measure fundamental properties of the neutron to unprecedented precision [2,3]. The most precise measurements of the neutron electric dipole moment [4] and the neutron β-decay lifetime [5–7] all employ UCNs in a trap. Any innovation that increases the storable UCN density and the deliverable UCN flux will simplify many technical difficulties in these challenging experiments. For example, a larger UCN density would reduce the size of most Electric Dipole Moment (EDM) experiments, making the implementation of stringent magnetic field uniformity and large electric field a less daunting task. In addition to applying UCNs for the studies of fundamental physics, there are many applications to condensed-matter physics and possible enhanced sensitivities derived from the long wavelength of UCNs [8], if a more intense source were to become available.

UCNs are already present in the Maxwell-Boltzmann spectrum of thermalized neutrons emerging from fission reactors. However, the percentage of the low-energy population is so low that even the most powerful research reactors cannot easily deliver high-enough UCN density to be of interest. The use of a cold-neutron moderator could shift the energy distribution to as low as 30 K, resulting in an increased UCN flux. In addition, many tricks have been implemented, including gravitational deceleration [9] and reflection using mechanical turbines [10], to further slow down neutrons. To increase the phase-space density beyond the limit imposed by the Liouville theorem, the most efficient method is to dissipate the neutron energy through excitations in condensed matter. Phonons in many materials have energies (of milli-electron volts) comparable to those of moderated cold neutrons. Golub and Pendlebury first proposed a "superthermal" source to use superfluid helium as a UCN converter [11]. In this type of source, the neutron gives up all of its kinetic energy by exciting collective excitations in the interacting material. The depletion of the UCN population via absorption of the same excitation energy (so-called "upscattering") can be suppressed to an arbitrarily small level simply by lowering the temperature of the converter. In the superthermal source, the number density of UCN could accumulate for durations as long as the β-decay lifetime of free neutrons.

*CL21@indiana.edu
†Currently at Department of Physics, Yale University, New Haven, Connecticut 06511, USA.

To preserve a sizable population of UCNs (∼milli-Kelvin) in a source environment of a few Kelvins, it is essential to avoid rethermalization by delaying upscattering. It is also important to control sources that could lead to UCN loss, such as nuclear absorption. Any medium possessing small nuclear absorption and significant neutron-scattering cross sections, regardless of the details of the excitation, are potential candidates. Successful implementations of this idea have been demonstrated in superfluid helium [12–14] and solid deuterium [15–18]. Both of these UCN converters have phonon excitations that match well with the incident cold neutrons for efficient energy transfer through single inelastic scattering. Other materials could potentially make even more efficient UCN converters. For one, ^{16}O has a neutron absorption cross-section five times smaller than that of ^{2}H. In addition to phonons, solid oxygen (s-O_2) in its low-temperature phases has strong magnetic interactions, which could be harnessed for UCN production [19]. These magnetic excitations have been widely studied using Raman scattering [20,21] as well as neutron scattering [22–24]. It has been shown that the low-temperature phases possess very different dynamics that often entangle translational, librational, and spin excitations through the orientation-dependent couplings between the diatomic oxygen molecules on the solid lattice sites.

We present an apparatus used to test s-O_2 as a UCN converter. A background subtraction technique was developed to enable collection of UCN production data in a pulsed-neutron facility, where the cold-neutron background can be significant. To extract the absolute efficiency of UCN production from the source, we carefully characterized the efficiencies of UCN transmission and UCN detection. We calibrated the efficiency of the apparatus using the well-studied solid orthodeuterium (o-$^{2}H_2$) as a standard reference. Here, we present a comprehensive test of the physics of UCN production in o-$^{2}H_2$ using this apparatus. The experimental results of UCN production in s-O_2 (including dependence on incident neutron energy, source volume, and the applied external magnetic fields) will be presented in forthcoming papers.

II. EXPERIMENTAL METHODS

A. Overview

The experiment is carried out on a cold-neutron beam line, where the cold-neutron flux and energy spectrum are well characterized. The neutron flux is collimated and monitored continuously. Even though the available flux is significantly smaller compared to previous experiments using a dedicated minispallation target [14,16], the removal of the uncertainties associated with the production and transport of the cold-neutron flux is essential in understanding the results of UCN production. The new apparatus consists of a neutron-scattering target cell, which allows us to grow the solid target *in situ*. The cell is placed in a cold-neutron beam line to act as the UCN production source.

UCNs, once produced inside the source, are extracted and then detected in a neutron detector placed sufficiently far away from the primary neutron beam. The strategic placement of the detector helps to control the backgrounds. Elastically scattered neutrons from the intense cold-neutron beam are the dominating source of background in this experiment. Determining the UCN extraction and transport efficiency is the major challenge in determining the absolute UCN production cross section. We therefore employ an o-$^{2}H_2$ as a UCN converter to benchmark the performance of the apparatus. Production of UCNs in o-$^{2}H_2$ was first demonstrated at the Petersburg Nuclear Physics Institute (PNPI) [25], and the superthermal behavior was quantified at the Los Alamos Nuclear Science Center (LANSCE) [15,16]. Further neutron transport and UCN production cross sections in o-$^{2}H_2$ have been carried out at Paul Scherrer Institut (PSI) [17,26] and by the Mainz/Münich group [18].

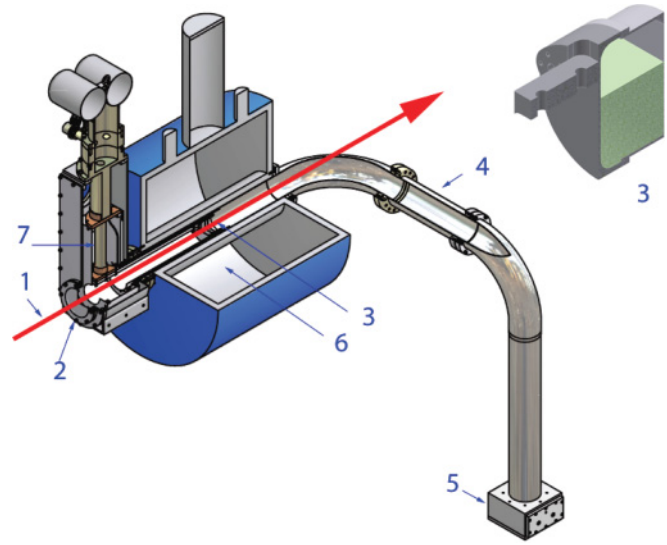

FIG. 1. (Color online) Schematic of the apparatus. Cold neutrons (1) enter the front aluminum window (2) and are incident on the cryogenic target cell (3). UCNs produced within the cell diffuse out of the cell and into a highly polished stainless steel UCN guide (4), which directs them through two 90-deg bends into a UCN detector (5). The cell itself resides in a 5.5-T (maximum) superconducting solenoid, housed inside a liquid helium cryostat (6). The target cell is cooled by a pulse tube refrigerator (7). A cutaway view of a partially filed cell (3) is shown in the inset.

A unique feature of the apparatus (illustrated in Fig. 1) is the integration of a high magnetic field, which allows for the study of magnetic excitations in s-O_2. The target cell is placed in the center of a superconducting (SC) solenoid with its axis aligned along the direction of the neutron beam. A cylindrical stainless steel guide serves as the UCN transport guide, as well as the insulating vacuum for the cryogenic target cell. The guide extends beyond the warm bore of the SC solenoid and connects to the rest of the UCN guide system.

The cell is larger than the cold-neutron mean free path (MFP) in o-$^{2}H_2$ so that the majority of incident cold neutrons scatter at least once before escaping the cell. Inside the filled cell, a small fraction of these scattering events, less than 1 part in 10^6, results in the production of UCNs. Some of the produced UCNs escape from the cell, enter the guide system, and move toward the detector.

The UCN guide system is made of stainless steel tubes 10.16 cm in diameter. The pharmaceutical-grade tubes are

internally electropolished to about ∼0.25-μm mean variation of the surface roughness. The total length is approximately 2 m with two 90-deg bends to direct the UCN perpendicularly out of the primary cold neutron beam, then vertically downward into the detector. The target cell is cylindrical, with the cold-neutron beam impinging on the front surface, and the UCNs are primarily extracted from the opposite surface downstream.

Ostensibly, only UCNs and very cold neutrons (VCNs), the latter with a lower probability, could totally reflect from the internal walls of the guide system and propagate to the detector. However, we find a significant background due to cold neutrons, which are diffracted and/or scattered incoherently by the section of UCN guide that intersects the beam. Even though the probability is quite low (∼3×10^{-8}), the large flux of cold neutrons passing through the apparatus leads to a background comparable to the UCN count rate. In Sec. IV, we show that this background can be removed by using its very distinct timing structure. With the relatively short guide system, the apparatus has a high UCN throughput, without being plagued by the cold neutron background.

Eventual use of s-O_2 as a UCN converter requires good temperature control of the cryogenic target cell, essential to reproducing the thermodynamic conditions for repeatable crystal growth. The major challenge arises from the reduction of the molar volume of s-O_2 by 12.5% upon cooling through the three solid phases (γ, β, α) at saturated vapor pressure. A discrete 5% change at the γ-β transition [27,28] at 44 K is the bottleneck for attaining large-sized s-O_2 cryocrystals in the β and α phases. Poor crystal quality, which adversely affects UCN extraction, needs to be controlled in order to gain understanding of the physics of UCN production in s-O_2. Density fluctuations (caused by cracks) over a range comparable to or larger than the UCN wavelength could result in additional scattering and lead to a reduced MFP [2]. Several groups have observed this effect in solid $^2H_2$. In particular, Atchison and coworkers [17] measured an ∼20-b increase of the total cross section in o-$^2H_2$ after several thermal cycles. There are no data on s-O_2.

Unlike o-$^2H_2$, the MFP of UCN in s-O_2 is not limited by the incoherent scattering length and is theoretically infinite because of the zero nuclear spin of the oxygen nucleus ^8O. On the other hand, any additional voids and cracks could limit the MFP of UCNs and significantly alter the extraction efficiency. With this apparatus, we have investigated different factors limiting the MFP of UCNs in the production target by changing the length of the target cell along the cold-neutron beam axis.

B. Cold neutron beam

The UCN production apparatus was constructed and tested at the Indiana University Cyclotron Facility and then installed on the Flight Path 12 (FP12) in the Lujan Center at LANSCE in August 2008. This neutron facility generates pulsed neutrons at 20 Hz from a spallation target. FP12 is coupled to a liquid-hydrogen neutron moderator with straight neutron guides. Details of the neutron-source emission-time distribution, guide performance, and overall intensity can be found in [29–31]. The neutron spectrum peaks at 3.3 meV (∼40 K) [32,33]. During the experiment, the neutron energy was determined from the time of flight (TOF), t, over the flight path length, L, by

$$E(t) = \tfrac{1}{2} m L^2 t^{-2}, \tag{1}$$

with the corresponding energy resolution (δE) of

$$\left(\frac{\delta E}{E}\right)^2 \approx 4\left(\frac{\delta t}{t}\right)^2 + 4\left(\frac{\delta L}{L}\right)^2. \tag{2}$$

Here, δt is the emission time, and δL is the uncertainty in the flight path length. The arrival of the proton pulse defines the t_0; however, details of moderator geometry, neutron slow down, and diffusion within the neutron source itself limit the timing resolution to the emission time [29]. The emission time is the time spread for neutrons of a given energy. The fastest neutrons observed by TOF are around 100 meV, with a resolution of around 2% for $\delta t \sim 150$ μs and $L = 21.1$ m. The relative uncertainty in the flight-path length is negligible. A frame-overlap chopper absorbs the long-wavelength neutrons and restricts the lower limit of the incident neutron energy to $E > 1.2$ meV. The most recent measurement [31] reported the neutron flux at the sample position to be $(2.0 \pm 0.1) \times 10^7$ n cm^{-2} s^{-1}, integrated over the spectrum from 1.2 to 20 meV, for 100-μA proton current on the spallation target. This measured intensity includes a boost in flux from an $m = 3$ guide.

Typical neutron spectra collected with our instrument on FP12 are shown in Fig. 2, using an empty cell and a cell filled with o-$^2H_2$ at 4.81 ± 0.02 K. The charge-integrated voltage signals from the cold-neutron monitors were digitized with a 12-bit waveform digitizer with a sample rate of 102.4 kHz. The neutron intensity $I(t)$ was normalized to the average proton beam current of 100 μA. A few features in the beam line modified the expected Boltzmann spectrum of neutrons

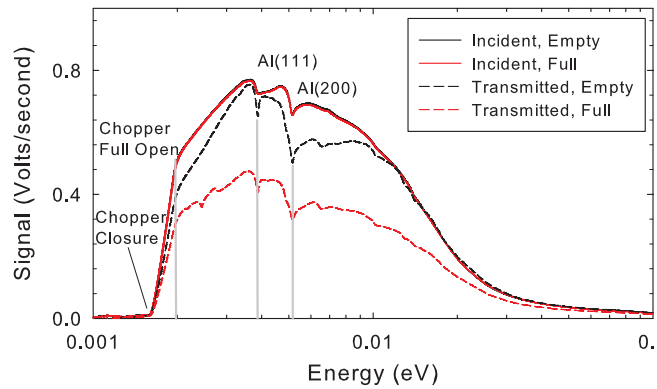

FIG. 2. (Color online) An example of the neutron monitor signals $I(t)$ with an averaged proton current of 100 μA on the spallation target. The empty cell signal (black) is compared with the filled cell (4 K o-$^2H_2$) data (red), for both the incident beam monitor (M_1) and the transmitted beam monitor (M_2). The solid gray lines label the Bragg edges and chopper opening that are aligned to determine the position of M_2 relative to M_1, which is fixed at 21.11 m. The vertical axis represents the voltage output from the amplifier, and its scale is set by a gain resistor in the amplifier circuit. The monitor signal $I(t)$ is the integrated voltage signal per time channel, normalized to the duration of data-taking for a nominal run (1000 s).

from the moderator. First, the signal was zero at low energies because the frame-overlap chopper was closed to prevent the slower neutrons from appearing in the next frame. The neutron flux increased as the chopper was opened, leading to a rising edge in the spectrum. The two most pronounced dips in the spectrum were the Al [111] and Al [200] Bragg edges from aluminum structural elements and vacuum windows in the cold-neutron beam path. Additional peaks appeared in the downstream monitor (M_2), owing to Bragg scattering from solid $^2H_2$ and the stainless steel UCN guides in our apparatus.

The neutron flux monitor M_1 was mounted at the end of the cold-neutron guide and was kept at a fixed position of 21.11 ± 0.03 m downstream from the moderator. By aligning the Bragg edges, we calibrated the position of M_2 to be 22.75 ± 0.04 m from the moderator, with the error bar on the distance determined from the width of the Bragg peak. Neutron signals measured by M_1 were unchanged between runs, indicating good stability.

The flux of transmitted cold neutrons (collected in M_2) was used to calculate the total scattering cross-section of the target material (o-$^2H_2$) during calibration runs. Several factors related to the nonideal geometry need to be taken into account in calculating the total cross sections. First, the cell was only partially filled with liquid o-$^2H_2$ (to a volume fraction $f = 0.601 \pm 0.014$) to avoid blocking the fill/vent line below solidification temperature and thus prevent pressure hazards. The fill volume was determined from the pressure drop in the storage volume, together with the known density of the liquid. With the cell uniformly illuminated, the neutron flux measured in M_2 thus consisted of both unattenuated neutrons from the upper part of the cell and the attenuated neutrons from the lower part of the cell. We determine the cross section using the following algorithm:

$$n\sigma(E)x = \ln\left[\frac{f}{(I_{\text{filled}}/I_{\text{empty}}) - (1-f)}\right], \qquad (3)$$

where σ is the total neutron cross section per molecule, n is the molecular number density, and x is the target thickness (3.56 cm for the calibration runs using $^2H_2$). The combined effects of digitizer voltage resolution and frame-overlap chopper restricted our measurement in the energy range from 1.2 to 30 meV.

The total cross section for o-$^2H_2$ is shown in Fig. 3, together with the data of Seiffert [34]. We obtain the best agreement with the previous measurements by adjusting the fill fraction to $f = 0.57 \pm 0.02$. This reduced value reflects the expected 4% fractional change of volume upon cooling o-$^2H_2$ to 4 K [35]. On the other hand, the volume change could also represent a (1.6 ± 0.7)-mm thick layer of solid frozen to the walls in the unfilled, upper portion of the cell. Given the high vapor pressure of o-$^2H_2$, both effects likely contributed to the filling fraction f smaller than that estimated by the record of pressure drop in the supply tank. The cell is about 1.6 MFP thick, and thus multiple scattering is likely to occur. Some already-scattered neutrons are scattered back into the small solid angle sustained by the entrance window of the detector. The enhanced transmission leads to a smaller cross section than the theoretical prediction. This effect would result in slight underestimation of the filling fraction.

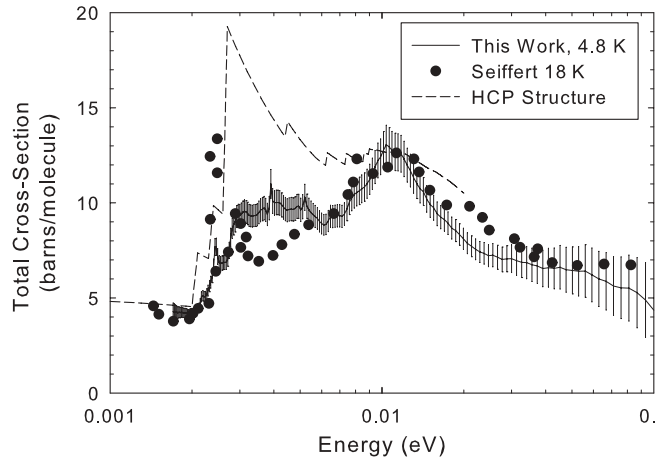

FIG. 3. The total cross-section of o-$^2H_2$ derived from Eq. (3) is compared with a previous measurement [34], along with the theoretical cross-section (dashed line) of solid $^2H_2$ in a hexagonal closed packed structure.

C. Gas handling system and cryogenic target cell

The materials of interest to this experiment, o-$^2H_2$ and O_2 gas, were highly volatile, and thus much care was put into the design and the construction of the gas handling system (GHS). A schematic of GHS is shown in Fig. 4. The GHS was constructed out of all stainless steel VCR tubing and connectors with all-metal seals. Only dry pumps and fomblin pumps were connected to the GHS. In the beginning of each run, it was cleaned by pumping until the pressures were less than 10^{-4} Pa (measured on the GHS panel) before any gas was introduced. The cell was filled from a 200-L storage tank via a flow controller on the GHS. A check valve was installed

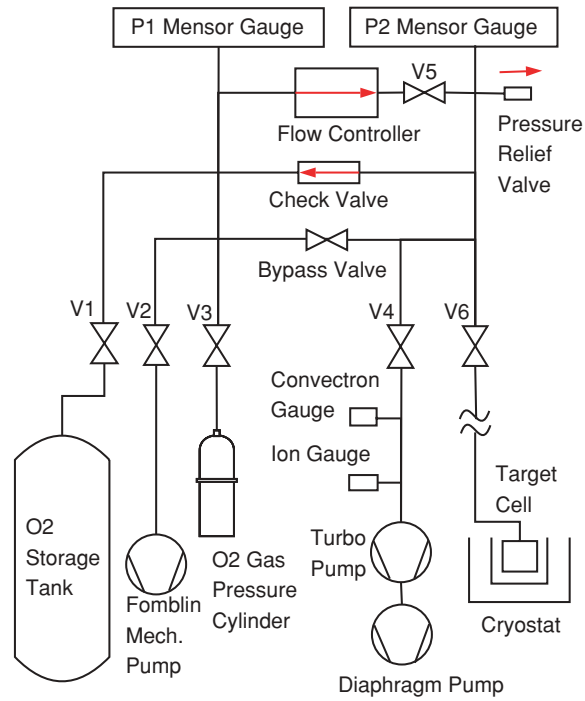

FIG. 4. (Color online) Schematic of the GHS.

between the cell and the storage tank. It was set to open at a differential pressure of 1.3×10^4 Pa to relieve overpressure in the cell back to the storage tank that contained the volatile gas. In addition, a dropout plate on the UCN guide system (which contains the cell) mitigated any catastrophic overpressure in the event that the cell should burst.

There was only one fill line (0.3175-cm-diameter SS tubing) that connected the GHS to the cell. In order to prevent blockage, the fill line had to be kept at temperatures above the solidification temperature of the material under study. In addition, the fill line was connected to the cryogenic cell using a stainless steel flange. The low heat conductivity of the stainless steel flange allowed for a large temperature gradient, isolating the cryogenic cell from the warm fill line. The fill line was wrapped with a nichrome wire heater and temperature controlled with a Proportional-Integral-Derivative (PID) loop.

Inside the cell, the solid was frozen from the liquid phase. The triple points are 18.7 K, 16.9 kPa for $^2H_2$ and 54.4 K, 152 Pa for O_2. The o-$^2H_2$ gas was borrowed from the dedicated UCN source for the UCNA experiment [36]. The ortho-para ratio of the gaseous $^2H_2$ was measured via Raman spectroscopy [37] at the beginning and the end of the experimental run. The initial measurements showed a contamination of $2.9 \pm 0.02\%$ para-$^2H_2$ and $0.17 \pm 0.11\%$ hydrogen deuteride ($^1H^2H$). The para fraction increased 0.2% over the 50-day duration of the experiment, and the $^1H^2H$ impurity level remained constant within error. After the $^2H_2$ calibration run, the $^2H_2$ gas was thoroughly pumped out before the oxygen gas was introduced. O_2 was supplied via a high-pressure gas cylinder at 99.999% purity.

The target cell was composed of a type-6061 aluminum cylindrical cup (several lengths available) bolted to a circular base flange and was installed horizontally in the magnet bore. The cell wall downstream of the beam direction was a thin aluminum window (0.254 mm) to facilitate UCN transmission and subsequent detection. To locate the cell within the center of the magnetic solenoid, the top flange was attached to one end of a high-purity (99.999%) aluminum bar ~30 cm in length. The aluminum bar was cooled by a pulse-tube refrigerator with a total cooling power of 1.5 W at 4 K. The target cell was made vacuum tight with an indium wire seal. Throughout the experiment, three different cell lengths were used with the base flange and cup combinations shown in Table I. The inner diameter of the cup side of the cell was 6.4 cm, and the base flange side was 6.67 cm. We used the medium cell for the o-$^2H_2$ calibration runs.

The cell was surrounded by two layers of cold shields. The inner cold shield was connected to the cold stage (cold head) of the pulse-tube refrigerator, while the outer shield was cooled by the warm stage (~50 K). The whole assembly was placed inside the stainless steel UCN guide, which run through the warm bore of a separate helium cryostat that housed the superconducting magnet. The inner cold shield was lined with a thin nickel foil (50 μm) to increase the collection efficiency of UCN emerging from the sides of the cell. Several G10 rings were used to center the cold shields and the cell, preventing thermal shorts between the cold shields and the inner wall of the UCN guide. Stable temperature operation with fluctuations no larger than 3 mK was achieved from 4.8 to 80 K with an empty cell. When filled, fluctuations of each temperature sensor increased to 15–20 mK. In addition, the temperature gradient across the cell when filled with solid o-$^2H_2$ increased to ~60 mK. The UCN guide was evacuated to less than 10^{-4} Pa to provide the insulation required to operate the cryogenic target cell. Throughout the experiment, a residual gas analyzer constantly assayed the gas composition in the guide vacuum to monitor for leakage from the cell.

TABLE I. Cell geometries used in the experiment (see inset in Fig. 1).

Cell type	Base length (cm)	Cup length (cm)	Volume (cm^3)
Small	1.143	0 (flat window)	38.82
Medium	1.143	2.413	117.4
Large	6.198	2.413	290.2

We used Lakeshore CERNOX 1050-SD resistive temperature detectors (RTDs) for thermometry because of their resistance to high radiation and insensitivity to high magnetic fields. A 100-W heater was attached to the aluminum cooling bar to adjust the cell temperature. Temperature readout and heater power was controlled using a Lakeshore 330 temperature controller. We developed a MATLAB-based Data Acquisition (DAQ) to implement slow controls for the RTDs, heaters, and pressure sensors. The same DAQ also controlled a fast digitizer to read output voltage signals from the cold-neutron monitors and the multichannel scalar (MCS) used to collect TOF spectrum from the UCN detector. This DAQ program provided a centralized platform for thermometry control and monitoring, data acquisition, visualization, as well as online data analysis.

III. RESULTS

A. Ultracold neutron detection

An improved version of the multiwire proportional counter [38] was used to detect UCN. Extensive neutron shielding using 0.5-m-thick borated polyethylene and B_4C powders surrounding the detector was essential to reduce the background rate from 300 Hz (un-shielded) to 134 ± 2 mHz. The counter, filled with 1 kPa of ^{3}He gas, had a small yet nonzero efficiency of 1.3% to detect cold neutrons with a 40-K Maxwellian spectrum. A typical UCN detector count rate was 612 ± 13 mHz with the target cell 60% filled with o-$^2H_2$ at 5 K and the spallation target incident with a 100-μA proton current. The beam-off ambient neutron backgrounds were only 20 mHz, and thus most of the 134 mHz observed was due to the transmitted cold neutrons that were elastically scattered in the UCN guide.

Inside the FP12 cave, there was a high level of γ radiation as a result of neutron captures. The γ's were detected by the UCN detector as low-energy pulses, but their intensity was high enough to prevent clean separation between the γ background from the higher energy neutron peak. We set the counter threshold to read the full-energy neutron peak. The large threshold enhanced γ rejection to nearly 100%, at a cost of reducing the efficiency for neutron detection to $85 \pm 3\%$

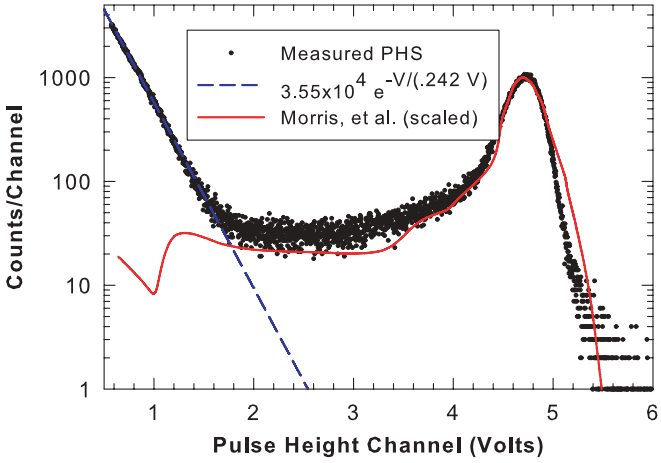

FIG. 5. (Color online) The pulse height spectrum measured by the multiwire proportional counter. Solid dots are the measured data. The red curve is the theoretical fit of the spectrum including the wall effects from the daughter nuclei of proton and triton. The solid blue line is the fitted γ background. With the threshold set to enclose only the full energy peak, the UCN detecting efficiency is 85± 3%.

(see Fig. 5). Note that the detector front window also attenuated the UCN flux, the effect of which was treated as a part of the transmission efficiency.

Signals from the UCN detector were recorded using a multichannel scalar (MCS), triggered by the proton pulse on the spallation target at 20 Hz. The UCN counts were recorded for 50 ms into the 512 time channels on the MCS. To collect enough data for statistical analysis, TOF spectra were accumulated by the MCS for 1000 s for each set of experimental conditions. Without the loss of proton pulses, 20 000 passes of spectrum were collected for each run. The first 1.2 ms of the detector response was dominated by the initial burst of radiation from the proton pulse and was cut in the analysis. The TOF of UCN to travel from the production cell to the detector was much longer (approximately several seconds) than the time between cold-neutron pulses (50 ms), so the UCN signal should have a uniform TOF spectrum. However, the measured TOF spectrum displayed several prominent peaks, as shown in Fig. 6. These peaks originated from the Bragg diffraction of cold neutrons from the stainless steel UCN guide that intersected the cold-neutron beam. The TOF information allowed us to associate the observed peak to the Bragg diffraction peaks. The width of the peaks resulted from the large angular acceptance of the UCN guide system. The guide was made of 316L stainless steel 3.175 mm thick. Its lattice structure is face-centered cubic with lattice parameter 3.6 Å [39]. Using a total flight path to the UCN detector of 24.5 m and scattering through an arc of 44 deg, we reproduced these peaks at the correct positions in the TOF spectrum. The expected and measured peak positions are summarized in Table II. In addition to these distinct peaks, there existed a long TOF tail that resembled the spectral shape of the incident cold-neutron spectrum. We attribute the long TOF tail to the incoherent elastic scattering of neutrons from the UCN guide.

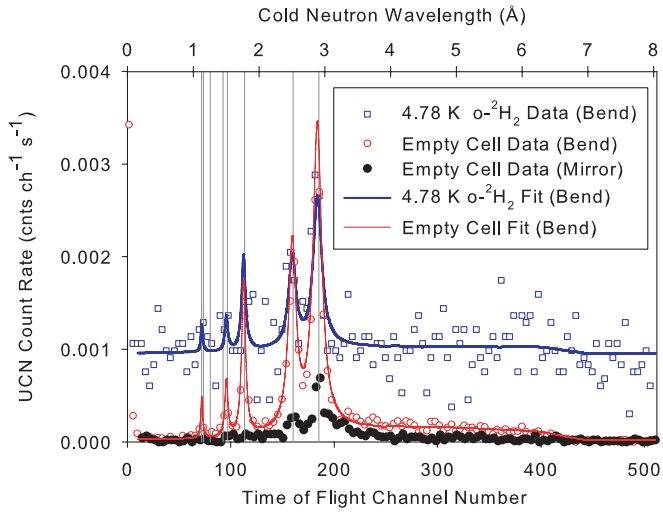

FIG. 6. (Color online) An MCS spectrum of the background collected with empty cell (red circles) is fitted to Eq. (5) (red curve). The grey vertical lines indicate locations of the first seven Bragg diffraction peaks from the stainless steel guide. When a mirror is used (black solid circles), the CN Bragg peaks drop in intensity, with some residual background scattered from the mirror's support frame and the vacuum chamber. UCN signal spectrum collected from the 4.8-K o-$^2H_2$ target is plotted (blue squares) and fitted to Eq. (5) (blue curve). Note the relative intensities of Bragg peaks of the filled and the empty cell. The reduced Bragg peak in the filled cell is a result of the attenuation of cold neutrons by the presence of o-$^2H_2$ solid.

To further reduce this source of background, we replaced the stainless steel bend with a 45-deg mirror made of a thin nickel foil only 0.127 mm thick, housed inside a stainless steel tee. This reduced the amount of background CN by an additional factor of four (from 134 mHz to 34.8 ± 1.3 mHz), but it also reduced the UCN transmission efficiency to 73 ± 2% of the previous configuration. Nevertheless, the signal-to-background ratio improved by more than a factor of two. The background TOF spectrum with the mirror is compared to that with the bend in Fig. 6.

TABLE II. The expected and observed locations of the Bragg reflections in the background spectrum for an Face-centered cubic (FCC) lattice, a = 3.6 Å. After re-binning, measurement wavelength resolution is ∼0.05 Å. The intensities of the [222] and [400] peaks were too low to be observed.

Indices	Expected Peak Å	Fitted Peak Å
1 1 1	2.89	2.90
2 0 0	2.50	2.52
2 2 0	1.77	1.78
3 1 1	1.51	1.51
2 2 2	1.44	–
4 0 0	1.25	–
4 2 0	1.12	1.14

IV. BACKGROUND SUBTRACTION

For the data obtained in the present geometry, a two-parameter fit to the cold-nuetron-induced background and UCN signal is implemented using the following procedure. First, the model used to fit the raw TOF spectrum is

$$\begin{aligned} C(t) &= C_{\mathrm{UCN}} + C_{\mathrm{bg}}(t) \\ &= C_{\mathrm{UCN}} + (B_{\mathrm{CN}}(t) + C_B) \end{aligned} \tag{4}$$

with

$$B_{\mathrm{CN}}(t) = \sum_{i=1}^{5} A_i^{\mathrm{coh}} \frac{1}{\pi} \frac{\frac{1}{2}\Gamma_i}{(t-t_i)^2 + \left(\frac{1}{2}\Gamma_i\right)^2} + A^{\mathrm{inc}}\phi(t). \tag{5}$$

Due to the long propagation time, the count rate of UCN, C_{UCN}, should be flat throughout the time channels. On the other hand, the CN background $B_{\mathrm{CN}}(t)$ has detailed, time-dependent features due to both coherent and incoherent scattering off the UCN guides. It can be modeled as the sum of distinct Bragg peaks (the five most prominent ones are included) and a continuous background due to diffuse scattering. The time-independent background C_B is introduced to account for the cosmic ray background and the detector electronic noise. In the analysis, the first ten channels are discarded to avoid contaminations from the prompt radiation created by the proton pulse on target. Occasionally, the proton pulse was observed to arrive earlier than the t_0 trigger, so we also cut the final two channels. The positions of the diffraction Bragg peaks are summarized in Table II. The peaks were fitted using Lorentzian functions with different width Γ_i and coherent amplitude A_i^{coh}, for $i = 1-5$. The widths could be quite large due to the large angular acceptance of the UCN guide geometry. The amplitudes A_i^{coh}, A^{inc}, and C_B are determined simultaneously in the final stage of the fit using χ^2 reduction techniques. Examples of MCS data and fitted spectra of a typical run are shown in Fig. 6.

Next, all data from background runs with an empty cell throughout the experiment are summed up to construct a parameterized background function $B_{\mathrm{CN}}(t)$, which is then used as a standard background function for UCN production runs. Much care has been taken in subtracting this background function from the UCN production data. With $^2H_2$ (or O_2) solid in the cell, the primary cold-neutron beam was attenuated due to elastic scattering, reducing the population of cold neutrons which could elastically scatter from the UCN guide. This resulted in a reduced cold-neutron background. On the other hand, cosmic ray and electronic noise characterized by C_B presumably remained constant between runs. Therefore, the background function used for UCN production runs is modified to be

$$C_{\mathrm{bg}}(f,t) = [(1-f) + fe^{-n\sigma(E(t))x}]B_{\mathrm{CN}}^{\mathrm{empty}}(t) + C_B, \tag{6}$$

where the cold-neutron-associated background function, $B_{\mathrm{CN}}^{\mathrm{empty}}(t)$, is derived from the empty-cell data (i.e., $C_{\mathrm{UCN}} = 0$), and f is the effective fill level discussed in Sec. II B. The function inside the bracket quantifies the overall attenuation of the CN background, and thus no arbitrary scale factor is required. The intensity of the diffraction peaks changed with varying level of fill inside the target cell, owing to the attenuation of cold neutrons by the scattering medium. This led to a self-shielding effect. The exponential dependence characterizes the energy dependence of the cold-neutron attenuation. The total cold-neutron scattering cross section, σ, was measured from the *in situ* cold-neutron transmission measurements (as discussed in Sec. II B), and x is the length of the cell.

The data are then fit to $C(t) = C_{\mathrm{UCN}} + C_{\mathrm{bg}}(f,t)$ through χ^2 minimization. To further increase counting statistics, different regions of interest (ROIs) are separated and rebinned individually. The ROIs are chosen to represent the distinct features of the data: the last 5 ms of the frame channels are mostly UCN and cosmic background only, whereas in the range from 25 to 40 ms the signal consisted of UCN and incoherent elastically scattered neutrons, and between 15 and 25 ms the signal is dominated by the diffracted neutrons. Six groups are fit separately, and the final determination of the free parameters is made via a grid-search algorithm that minimizes the combined χ^2, defined as

$$\chi^2 = \sum_{i=1}^{6} \frac{[(C_{\mathrm{Meas}} - C_{\mathrm{Fit}})_i]^2}{\sigma_i^2}, \tag{7}$$

where σ_i is the statistical uncertainty in the ith group. Typically, the reduced χ^2 is close to 1, and no larger than 1.5. The χ^2 distribution is consistent with expectations. Nominal results of the fit are shown in Fig. 6 for a measurement using o-$^2H_2$ at 4.78 K.

In the final minimization procedure, only f and C_{UCN} are left as free parameters. A typical scan of χ^2 in the parameter space is shown in Fig. 7, which presents the analysis of a data set collected using solid $^2H_2$ at 4.78 K. The result shows a low degree of correlation between C_{UCN} and f, reflecting that the UCN count is not significantly altered by changing the background level through adjusting the fill level f. The minimized χ^2 is 1.26 for this temperature.

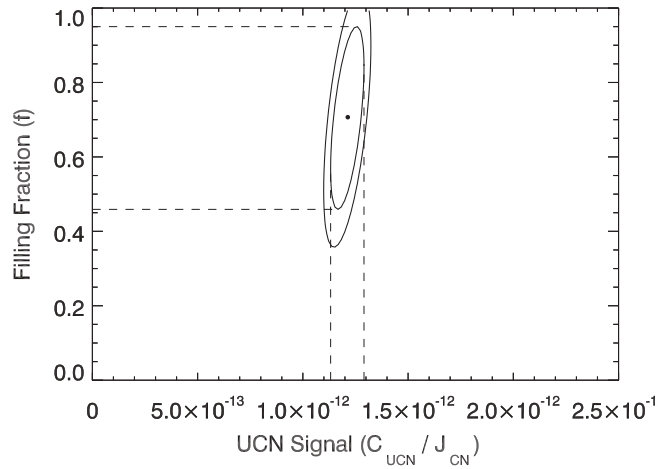

FIG. 7. A scan of χ^2 for the 4.78-K measurement. The dot indicates the location of the minimum, at reduced $\chi^2 = 1.26$, surrounded by the contours which enclose the 68% and 95% confidence levels. A narrow range of UCN signal is determined across a wider range of filling fractions, indicating the relative in-sensitivity of the extracted UCN signal to the f parameter.

However, if one sets the filling fraction to 1, the minimized χ^2 rises to 1.70, indicating a poor fit to the data. The averaged filling fraction across all temperatures is $f = 0.61 \pm 0.06$ (with the uncertainty determined from the standard deviation across the data points at different temperature), consistent with the value estimated from the total cross-section estimate and the pressure change in the gas storage tank. Error bars on the values of C_{UCN} and f are set by the largest extent of the 68% confidence level ($\Delta\chi^2 = 1$) in determining each free parameter. For each 1000-s run, the UCN count rate can be measured to within 8% relative uncertainty.

To facilitate the comparison of UCN production between runs with different operational conditions, we define the normalized UCN signal, S, as the total UCN count rate (C_{UCN} determined from the fitting routine) normalized to the incident cold-neutron current, J_{CN}, and the molar quantity of material under study, N_{mol}:

$$S = \frac{1}{N_{\mathrm{mol}}} \frac{C_{\mathrm{UCN}} \times 512}{J_{\mathrm{CN}} f}. \tag{8}$$

Here J_{CN} is the number of total neutrons passing through the cell per unit time, normalized to 100 μA of the proton beam on the spallation target. It is related to the neutron flux by $J_{CN} = A_{\mathrm{cell}}\phi J_{\mathrm{CN}} = A_{\mathrm{cell}}\phi$, where A_{cell} is the area of the beam incident on the production cell and ϕ is the cold neutron flux. J_{CN} is calculated from the neutron signal measured by the cold-neutron monitor M_1, multiplied by the ratio of the cross-sectional area of the cell and that of the monitor. The filling fraction f accounts for the fact that not 100% of the incident cold neutrons are intersecting with the target. The UCN count rate, C_{UCN}, has units of count rate per channel. To calculate the total count rate, it is thus multiplied by the total channel number, 512, which corresponds to the whole 50 ms in time. Normalizing the UCN count rate to the neutron flux monitor is a more robust method than normalizing to the proton beam current, as this avoids introducing additional uncertainties from the inevitable varying conditions in the liquid-hydrogen cold-neutron moderator (such as temperature, fill level, and ortho/-para ratio).

Since the cold-neutron detectors (M_1 and M_2) are operated in the current-integrating mode, there is an additional step required to convert the detector signal $I(t)$ to the cold-neutron current J_{CN} passing through the cell. The total neutron current ranging from 1.5 to 20 meV is determined by:

$$J_{\mathrm{CN}} = k \sum_{19.5\mathrm{ms}}^{29.3\mathrm{ms}} I(t_i), \tag{9}$$

where $I(t_i)$ is the digitized voltage -signal output from the neutron detector in the ith time channel. The calibration scaling factor,

$$k = (7.17 \pm 0.04) \times 10^5 \quad \frac{\mathrm{neutrons}}{\mathrm{volt}}, \tag{10}$$

is determined by setting the total neutron flux to the results of the most recent flux measurement in FP12 [31]. This measurement used a ^{235}U fission chamber and reported a total neutron flux of 2.0×10^7 cm^{-2} s^{-1} (with 100 μA of proton current) over the energy range of interest to UCN production (i.e., 1.5 to 20 meV). Note that in Eq. (9), only part of the measured TOF spectrum (between 19.5 to 29.3 ms, i.e., 2.7 to 6.0 meV) is used to determine the scaling factor k. The electronic interference from adjacent power lines (40 A) that supply the pulse tube refrigerator compressor introduced additional noise, and thus the time channels with low neutron currents are excluded from the summation.

A simple analysis that subtracts the background using the empty-cell data tends to overestimate the background for reasons previously mentioned. However, for later runs in which the nickel foil mirror replaced the bend in the neutron guide, the background was significantly reduced, and the simple background subtraction routine produces signals in reasonable agreement with the algorithm presented previously. The simple subtraction approach uses the model:

$$S_{\mathrm{simple}} = \frac{1}{N_{\mathrm{mol}}} \frac{\Sigma_i (C_i - C_B) - \bar{T}\Sigma_i (B_i - C_B)}{J_{\mathrm{CN}} f}, \tag{11}$$

where $\Sigma_i C_i$ is the total number of counts measured with a filled cell and the background $\Sigma_i B_i$ is the total number of counts measured with an empty cell. As mentioned before, the first few channels that are contaminated by the prompt pulse are excluded from the sum. The reduction of the background from the self-shielding effect due to the presence of the UCN production medium is captured by the transmission fraction, $\bar{T}$, averaged over the incident cold-neutron energy spectrum. To properly account for the fact that not all cold neutrons were attenuated uniformly by a cell partially filled to fraction f, the transmission factor is calculated as

$$\bar{T} = (1 - f) + f \times \frac{\int e^{-n\sigma(E)x} \phi(E) dE}{\int \phi(E) dE}, \tag{12}$$

where $\bar{T} = 0.651$ for the "bend" measurement ($f = 0.57$) and $\bar{T} = 0.691$ for the later "mirror" measurement ($f = 0.507$).

With the proper background subtraction, we can construct a figure of merit to compare different guide geometries. Comparison of the signal-to-noise ratio (SNR) between the mirror and the bend guides can be made using

$$SNR = \frac{S}{\bar{T} B}. \tag{13}$$

For the bend, the SNR is 5.6, and it improves significantly to 12.5 using the mirror. The experimental results from both approaches are displayed in Fig. 8. Results using the non-linear fitting algorithm are within the error of the simple subtraction method. The subtraction method is most useful when counting statistics for each individual TOF channel is low, such that integration over all channels is required to generate a better statistical confidence in the UCN signal. The agreement between the two approaches warrants the adoption of the simple background subtraction method for the forthcoming analysis on s-O_2, in spite of the rather unusual background shape.

The data in Fig. 8 were taken using o-$^2H_2$ in a 3.556-cm-long (117.4-cm^3) cell with bend and mirror. The solid was cooled over 14 h starting from the liquid phase. In the liquid phase at 20 K, there was already a non-zero number of UCN detected well above the background level. Solidification began at the triple point at 18.7 K. The observed UCN counts

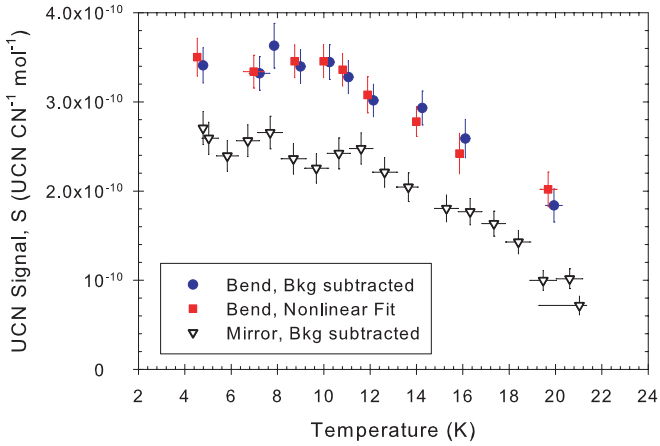

FIG. 8. (Color online) UCN production in condensed o-$^2H_2$. The removal of the scattered cold-neutron background by the fitting procedure (red squares) is commensurate with a simple background subtraction approach (blue circles). To show the difference between the two data sets, the blue circles are off-set in temperatures by 0.25 K. The replacement of the bend by the mirror (open triangles) reduces the UCN transmission by 27%.

increased monotonically as the temperature of the production target decreased until a saturation was reached around 10 K. The enhanced UCN production was expected as the MFP of UCN increased with the reduction of the thermal phonon population, leading to a suppressed rate of upscattering loss. The saturation can be understood primarily by the reduction of upscattering at lower temperatures to the limit in which the escape length of UCN became comparable to the upscattering length. In addition, cold-neutron scattering out of the cell by the UCN source was enhanced due to the increased density of the cold solid.

V. DISCUSSION

We build a Monte-Carlo code on the GEANT4 framework [40], with a complete geometry of the experiment to simulate the UCN yield using relevant UCN cross-sections. The simulation applies the physics of UCN production in o-$^2H_2$, and assumes simple transport processes to track UCN from the source, through the UCN guide, and into the UCN detector. We simulate the expected UCN production using modest assumptions on the material properties (such as guide surface reflection specularity, UCN upscattering cross-section in $^2H_2$, etc.). We then compare the measured UCN signal $S_{\rm meas}$ to the simulated UCN signal $S_{\rm sim}$, defined in Eq. (8) to fine-tune the guide parameters. Furthermore, the guide parameters were constrained with additional data from UCN transmission measurements of our guides using the UCNA source. In the simulation, we assume all guide sections have the same surface qualities, to reduced the number of free parameters.

The simulated UCN count rate $C_{\rm sim}$ can be presented as a function of the various efficiencies through different parts of the apparatus:

$$C_{\rm sim} = \varepsilon_{\rm elec}\varepsilon_{\rm trans}(n V_{\rm source}\phi_o\bar{\sigma}), \tag{14}$$

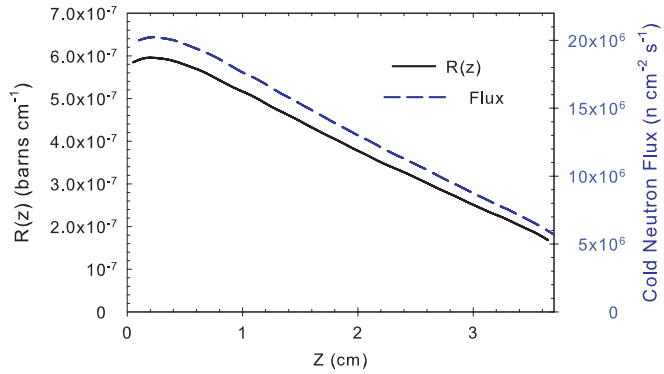

FIG. 9. (Color online) Position dependence of the UCN production rate, calculated using Eq. (16). The evolution of the integrated cold-neutron flux through the volume is also shown (right vertical axis).

where $\varepsilon_{\rm elec}$ is the detector efficiency, $\varepsilon_{\rm trans}$ is the transport efficiency for a UCN to travel from the source through the guide system and finally to the detector active volume, n is the molecular number density, and $V_{\rm source}$ is the volume of o-$^2H_2$ illuminated by the cold neutrons. The cross-section $\bar{\sigma}$ is the UCN production cross-section averaged over the incident cold-neutron spectrum:

$$\bar{\sigma} = \frac{1}{\phi_o}\int_0^{1\ \mu\rm eV} dE_{\rm UCN}\int_0^{20\ \rm meV} dE\phi(E)\sigma(E\rightarrow E_{\rm UCN}). \tag{15}$$

To include the detectable VCN signal, the integration includes neutrons with energies up to 1 μeV. Note that the transmission efficiency depends on the neutron energy. As shown in Fig. 10, some VCNs with energiesy larger than the Fermi potential of the UCN guide can be present among the detected signals.

A. Spatial distribution of UCN production

Over the energy range relevant to UCN production, the elastic MFP of the cold-neutron beam varies from 2.8 to 5.6 cm. Since the cell length is comparable to the elastic MFP, a large probability of elastic scattering of the incident cold-neutron beam inside the cell is expected. This would significantly alter the spatial distribution of the cold-neutron flux. The spatial distribution is modeled using another Monte Carlo code (MCNP5 [41]). The code simulates the multiple-scattering process of each cold neutron and tracks the evolution of the cold-neutron flux throughout the target cell. A large fraction (~50%) of cold neutrons experienced at least a single scattering, and may downscatter to UCNs before escaping the o-$^2H_2$ volume. The results of the simulation can then be compared to the measurements of the transmitted cold-neutron beam collected by the detector M_2 (Sec. II B).

To account for this spatial variation of the cold-neutron flux, a position-dependent UCN production rate, $R(z)$, is defined which varies as the distance, z, along the symmetry axis of the cylindrical cell. To explore the position dependence, the target cell is subdivided into slices and the production rate is averaged over the energy spectrum of cold neutrons in each

individual slice, that is,

$$R(z) = \frac{1}{\delta z} \frac{\int_z^{z+d_z} dz \int_o^\infty dE \sigma(E \to E_{UCN}) \phi(E, \vec{r})}{\int_0^L dz \int_o^\infty \phi(E, \vec{r})}. \quad (16)$$

This calculation includes a divergence of the neutron beam of 0.5 deg at the guide exit (a result derived from another simulation using VITESS [42]). The UCN production cross-section, $\sigma(E \to E_{\rm UCN})$, used in the calculation is from the work of [26], integrated over final-state UCN energy up to 1 μeV. Note that there are uncertainties in the cross-section quoted in [26], as the data were scaled to agree with a calculation based on the simple Debye model and the incoherent approximation. The production rate is summed over each volume segment dV_z, defined as the cross-sectional area of the cell multiplied by the thickness dz. The incident neutron spectrum, $\phi(E, \vec{r})$, used in the Monte Carlo is measured by M_1.

The position-dependent UCN production rate, $R(z)$, and the cold-neutron flux, $\phi(z)$, are shown in Fig. 9, at a resolution of $\delta z = 1$ mm. Results of the simulation show that the cold-neutron energy spectrum is not significantly altered by the presence of o-$^2H_2$, however, the intensity decreases along the length of the cell as more cold neutrons are elastically scattered out of the cell. Notice that the spatial distribution does not follow a simple exponential decay, probably due to the fact that the cell is of finite volume. Finally, the cold-neutron flux peaks at a few millimeters into the cell because of the locally enhanced cold-neutron population through accumulation of elastically scattered neutrons and the increase of the neutron flux in the adjacent volume slices around the scattering site. This spatially-dependent production rate function is then used to generate the UCN source term in the GEANT4 simulation.

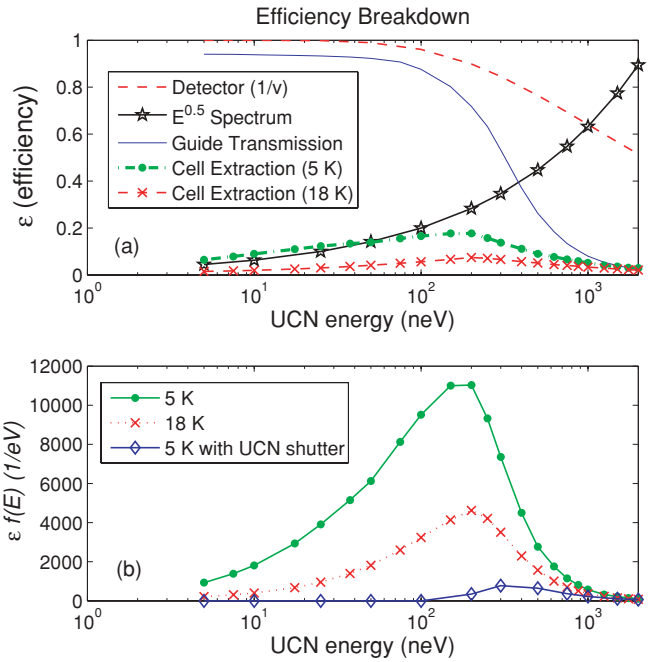

FIG. 10. (Color online) (a) A breakdown of efficiencies of UCN transport in the apparatus as a function of UCN energy. (b) UCN transport efficiency weighted by the production spectrum $f(E)dE \propto \sqrt{E}dE$. The energy-averaged efficiency can be estimated by integrating the curves up to the maximum energy of interest. The blue curve is the efficiency of neutron transport through a UCN shutter used later in the experiment.

B. UCN transport efficiency

The total transport efficiency of UCN through the apparatus can be divided into three independent components: efficiency of extraction from the cell, efficiency of transport through the guide system, and efficiency of the UCN detector. The target cell, cold-shield, and nickel shield lining are modeled using the known absorption and scattering cross-sections. The upscattering of UCN in these guide materials is assumed to be negligible due to their low temperatures and small thicknesses. Among all the volumes sampled by UCN, the $^2H_2$ target cell is the greatest source of loss. Inside the cell, the diffusivity and additional elastic cross-sections are difficult to constrain. Reasonable assumptions about the magnitudes of the various parameters are made, and a comprehensive simulation is used to assess the sensitivity of the efficiency to these parameters. Whereas the elastic scattering can be studied using GEANT4 simulations and the absorption loss in solid $^2H_2$ is well known, the upscattering cross-section depends on the model employed. We demonstrate that discrimination between different models is possible using our experimental data.

To this end, a UCN transport Monte Carlo based on GEANT4 is used, which includes all of the UCN transport physics. UCNs are created inside the cell according to the spatial distribution discussed above [Eq. (16)]. The initial UCN spectrum is proportional to $v^2dv \sim \sqrt{E}dE$. Neutrons with energy up to 1 μeV are tracked. The stainless steel UCN guide walls have a neutron potential energy of 189 neV, and 1% diffusive surfaces. The loss per bounce used in our guide model is 8.5×10^{-5}. Imperfections due to welding are measured to be 2.5-cm-long rings at the interface between the guides and conflat flanges and are modeled in the Monte Carlo as 100% diffusive regions of the guide. The foil loss is characterized in a followup experiment to measure the guide transmission using UCNs from the UCNA solid $^2H_2$ source. The UCN intensity in the guide system with and without the nickel foil mirror inside a stainless steel tee in place was measured, and the results are used to constrain the guide parameters. The microscopic details of UCN scattering off material surface vary greatly over different scenarios. It should be cautioned that the physics implemented in the GEANT4 code do not apply to every surface. However, lacking a more general model and simulation tools, we proceed with using the simple two-parameter model [2] to treat the surface scattering. Within this framework, the diffusivity of the foil is determined to be ~40%, with which the simulation reproduces the transport reduction of 73% when the 90 deg bend is replaced by the nickel foil mirror.

Finally, the loss in passing through the detector window (a 0.51-mm aluminum foil) is not negligible. A transmission efficiency through the foil of 50% for a 1-m vertical drop was measured at the UCNA source, using a configuration similar to the vertical guide in our system [38]. The result indicates that there exists significant loss beyond the typical absorption and elastic scattering in aluminum. The diffuse elastic scattering

in the aluminum foil is tuned to produce UCN transmission that agrees with this measurement.

Detailed results from the simulations reveal that about 3/4 of the UCNs produced are lost before escaping the cell. The loss of UCN occurs mostly on interaction with the cell body, which is made of aluminum. Aluminum was used to construct the cell body for its low Fermi potential and the ease of UCN extraction, however, its large neutron absorption cross-section is a serious source of UCN loss. For a UCN with velocity of 5 m/s, only 18% of the UCN population survives losses in the target cell and passage through the thin aluminum front window. In addition to the loss in the aluminum cell body, 14% of the UCN flux is lost in the solid $^2H_2$ at 5 K, due mostly to upscattering. Upscattering loss increases to 66% at 18 K.

Furthermore, the survival probability of UCN through the cell is a function of the UCN energy. The maximum cell-extraction efficiency is 0.15 for UCNs of 200 neV. Over the integral UCN spectrum up to 1 μeV, the cell-extraction efficiency at 5 K is found to be 0.07, which is the fraction of produced UCNs that emerge from the cell, travel through the cold shield, and enter the guide. The transport efficiency through the guide is also energy-dependent. With a typical $\cos(\theta)$ angular distribution (Eq. (2.68) in [8]), the probability to transport a continuous UCN spectrum (up to 1 μeV) through the guide to the detector window is 0.31. Together with the transmission of 0.50 through the detector window, the ^{3}He$(n,p)^3$H reaction probability of 0.86, and the full energy peak efficiency of the detector of 0.85, one estimates an overall detection efficiency of 0.008. The efficiencies for UCN transport and detection are listed in Table III.

C. UCN upscattering

The temperature dependence of UCN production originates solely within the production source. The UCN upscattering cross-section depends strongly on temperature of the source. The density of the target material also changes with temperature, but the dependence is much weaker by comparison. Using the upscattering cross-section calculated in our previous work [43], our simulations did not reproduce the experimental data. In particular, the simulation predicted saturation at a much lower temperature of around 6 K. This calculation used the incoherent approximation (IA) that treats the coherent inelastic scattering in the same fashion as the incoherent inelastic scattering.

TABLE III. Efficiency breakdown and UCN production estimates. Presented numbers are spectral-weighted efficiencies and cross-sections for UCNs with a continuous energy spectrum up to 1 μeV to include the VCN population, and for UCNs with energies up to the 300 neV in the guide, after the energy boost of 104 neV upon exiting $^2H_2$.

Parameters	0–1 μeV	0–300 neV
Cell extraction	0.07	0.15
Guide transmission	0.31	0.80
Detector window transmission	0.50	0.50
^{3}He$(n,p)^3$H probability	0.86	0.97
$\varepsilon_{\text{elec}}$ (total energy peak)	0.85	0.85
Total efficiency	0.008	0.05
$\bar{\sigma}$ (b)	1.42×10^{-6}	1.27×10^{-7}
N ϕ_0 (cm^{-2} s^{-1})	$(44 \pm 3) \times 10^{30}$	
Expected rate (s^{-1})	0.49 ± 0.03	0.28 ± 0.02
Measured rate (s^{-1})	0.48 ± 0.05	

In evaluating the cross-section for incoherent scattering, the density of states is used to weigh the contribution of the different phonon modes. While the IA works quite well to estimate the total cross-section, it might not be appropriate when evaluating cross-sections for UCN scattering processes, in which the phase space of scattering is significantly limited. The lack of detailed Q- dependence in the IA leads to significant errors in calculating the UCN cross-sections. For hydrogenous neutron moderators ($\sigma_H^{\text{coh}} = 1.7583$ b, $\sigma_H^{\text{inc}} = 80.27$ b), the IA has small uncertainties. In the case of o-$^2H_2$, the contribution of coherent scattering is not small ($\sigma_{^2H}^{\text{coh}} = 5.592$ b, $\sigma_{^2H}^{\text{inc}} = 2.050$ b), and the validity of IA is questionable. To address this concern, a new calculation is implemented, using a full model that includes spin statistics and coherent inelastic scattering, as well as the incoherent scattering. This new calculation revises the UCN upscattering cross-section to be a factor of two to four times smaller than the calculation using the incoherent scattering [44].

Using the updated upscattering cross-section calculated based on the full model of the dynamic structure function $S(\vec{Q}, \omega)$ for o-$^2H_2$ [44], the Monte-Carlo simulation produces a temperature dependence of UCN production that agrees better with the experimental data. Figure 11 shows both models, along with the background-subtracted data for the bend and mirror measurements. To accentuate the temperature dependence, these two sets of data and the simulation results

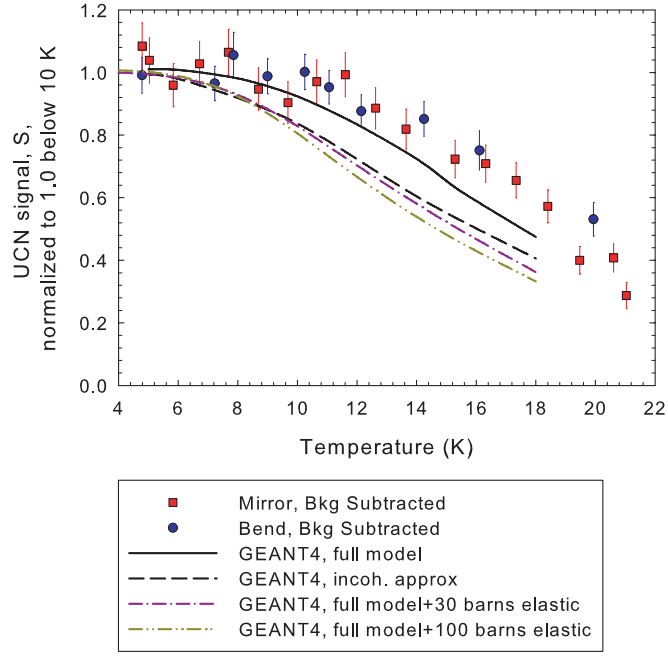

FIG. 11. (Color online) Results of o-$^2H_2$ UCN production experiment and GEANT4 simulation. Simulation parameters (guide efficiency, production, etc.) are detailed in the text.

are scaled to agree at 4.78 K (where upscattering is small in both models) to eliminate the effects on guide transmission in the different experimental configurations. At temperatures higher than 12 K, where the UCN upscattering cross-section is quite large (>2 b), the incoherent model is excluded at the 1 σ level and larger. Other effects that lead to increased elastic scattering inside the source, such as cracks and voids leading to inhomogeneity scattering, have been studied, however, the higher saturation temperature can only be explained by reduced upscattering cross-sections.

Increasing the elastic scattering inside the UCN production source would lead to local trapping of UCN and thus amplify the effects of any loss mechanism inside the source. This effect will result in a steeper temperature dependence on the UCN production data (simulated results are plotted in Fig. 11). The solid $^2H_2$ was solidified from liquid and cooled slowly over the duration of 10 h without any deliberate thermal shock. In order to quantify the elastic scattering of UCN due to the presence of inhomogeneity, one needs to carry out measurements of UCN MFP by systematically varying the cell dimensions. We have done this study on the solid O_2 target but did not perform it with solid $^2H_2$. On the other hand, comparing the experimental data with GEANT4 simulations with varying degrees of UCN elastic scattering suggests that the inhomogeneity scattering of UCNs inside the production target is no more than a few barns. This can be compared to the minimum elastic-scattering cross-section, arising from incoherent elastic scattering, which is about 2 b. This result is consistent with the findings of the Los Alamos and PSI experiments on solid $^2H_2$ sources, which are consistent with modest variations in the effective elastic-scattering cross-section for typical solid $^2H_2$ crystal growth.

We also surveyed experimental results on UCN production using solid deuterium reported independently by various research groups in Fig. 12. While the results of simulation using the updated upscattering cross-section agree quite well with our data and the data set measured at PSI, the data sets from the LANL and Mainz groups show a much steeper temperature dependence for temperatures higher than 10 K. The difference comes from the different source configurations. In these two experiments, solid $^2H_2$ was condensed from vapor at the end of the UCN guide, which was cooled below the solidification temperature of $^2H_2$. The source was designed to reduce the transmission loss by eliminating the vacuum window that is typically installed to contain the volatile $^2H_2$. The windowless source worked quite well at low temperatures, however, for temperatures higher than 10 K, the entire UCN guide was filled with $^2H_2$ gas at the saturated vapor pressure. The large upscattering cross-section from the $^2H_2$ vapor, together with a large volume where the vapor permeated, resulted in a temperature dependence steeper than the simple prediction where UCN upscatter through absorption of phonon in the confined region of the source. Both PSI and our experiment used $^2H_2$ contained in a cryogenic cell, in which the vapor region was considerably smaller. None of the data sets showed a low saturation temperature, as predicted by the IA. Instead, the universal temperature dependence observed in independent experiments agrees better with results of the simulation using upscattering cross-sections predicted by the full model.

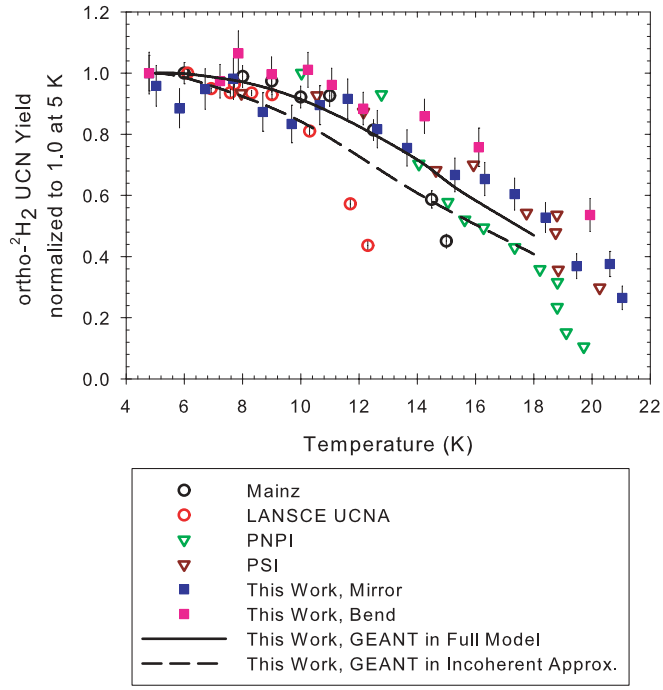

FIG. 12. (Color online) The temperature dependence of this experiment compared to similar experiments (Mainz [45], LANSCE UCNA [15], PNPI [25], and PSI [17]). All data are scaled to unity at 5 K.

To summarize, in this work the essential focus is to use solid o-$^2H_2$ as a source to calibrate the overall efficiency of the apparatus to detect UCNs. In these calibration runs, the absolute count rate of the UCN detector can be estimated using Eq. (14):

$$\text{Count rate} = \varepsilon_{\text{trans}}\varepsilon_{\text{elec}} N \phi_o \bar{\sigma},$$

where $N = n \times fV = 3 \times 10^{22}$ cm^{-3} $\times (0.60 \pm 0.03) \times 117$ cm^3 $= (2.2 \pm 0.2) \times 10^{24}$ is the total number of $^2H_2$ molecules in the cell. With 100-μA proton beam current on the spallation neutron target, the cold-neutron flux integrated over the UCN production cross-section is

$$\begin{aligned}\phi_0\bar{\sigma} &= (2.0 \pm 0.1) \times 10^7 \text{ cm}^{-2} \text{ s}^{-1} \ (1.42 \times 10^{-6} \text{ b}) \\ &= (28 \pm 1.4) \times 10^{-24} \text{ s}^{-1}.\end{aligned}$$

Here the UCN production cross-section, $\bar{\sigma}$, is estimated following Eq. (15) using our updated calculation, which includes the coherent scattering process. Note that the production cross-section reported in [26] was normalized to each atom and did not include either the spin statistics or the rotational form factor for molecular deuterium; the cross-section independently reported in [46] should be corrected by a factor of two to properly account for the kinematic range of momentum transfer through $-q_{\text{UCN}}$ to $+q_{\text{UCN}}$. With the total detection efficiency of 0.008, the expected neutron count rate is 0.49 $\pm$ 0.03 s^{-1}, which agrees with the measured count rate of 0.48 $\pm$ 0.05 s^{-1}. This confirms the general validity of our model of UCN transport.

VI. CONCLUSION

An apparatus to produce and measure UCNs from different converter materials has been constructed, the details of which have been presented in this article. To allow for meaningful measurements in a pulsed-neutron beam line, a background-subtraction technique has been developed to extract UCN production data on top of a high level of background from cold-neutron scattering. Using neutrons on FP12 at LANSCE, we have measured the transport efficiency of the apparatus using solid o-$^2H_2$ as a calibration source. Successful application of a Monte Carlo model, which includes detailed physics of cold-neutron attenuation, UCN upscattering, and inhomogeneity scattering describes the data reasonably well. With our detailed understanding of the apparatus, the analysis can be extended to UCN production in s-O_2, where the production rate has never been carefully quantified. The results of UCN production in s-O_2 using this apparatus will be reported in forthcoming papers. Finally, the calibration data shows evidence for a reduced UCN upscattering cross-section in solid o-$^2H_2$ as indicated by the higher saturation temperature. With the updated UCN upscattering cross-section calculated using a full coherent scattering model that remedies the shortcomings of the widely-adopted IA [44], the simulation agrees with the experimental data on UCN production in solid o-$^2H_2$ over the temperature range from 5 K to 18 K.

ACKNOWLEDGMENTS

We thank Phil Childress, Jim Bowers, Darren Nevitt, and Todd Sampson in the Indiana University physics shop for their rapid, high-quality fabrication of equipment used in this experiment. We thank Bill Lozowski for his effort in preparing the nickel-coated guides. We are also grateful for the assistance provided by the Lujan Center and LANSCE. We acknowledge Shah Vallilopy for performance of the VITESS simulation of guide divergence. This work was supported by NSF Grants 0457219 and 0758018.

[1] P. Ageron, W. Mampe, and A. I. Kilvington, Z. Phys. B **59**, 261 (1985).
[2] R. Golub, D. J. Richardson, and S. K. Lamoreaux, *Ultra-cold Neutrons* (Taylor & Francis Group, New York, 1991).
[3] H. Abele, Prog. Part. Nucl. Phys. **60**, 1 (2008).
[4] C. A. Baker *et al.*, Phys. Rev. Lett. **97**, 131801 (2006).
[5] W. Mampe, P. Ageron, C. Bates, J. M. Pendlebury, and A. Steyerl, Phys. Rev. Lett. **63**, 593 (1989).
[6] S. Arzumanov, L. Bondarenko, S. Chernavsky, W. Drexel, A. Fomin, P. Geltenbort, V. Morozov, Y. Panin, J. Pendlebury, and K. Schreckenbach, Phys. Lett. B **482**, 15 (2000).
[7] A. P. Serebrov *et al.*, Phys. Rev. C **78**, 035505 (2008).
[8] R. Golub, Rev. Mod. Phys. **68**, 329 (1996).
[9] Y. Y. Kosvintsev, E. N. Kulagin, Y. A. Kushnir, V. I. Morozov, and A. V. Strelkov, Nucl. Instrum. Methods **143**, 133 (1977).
[10] A. Steyerl, Nucl. Instrum. Methods **125**, 461 (1975).
[11] R. Golub and J. M. Pendlebury, Phys. Lett. A **53**, 133 (1975).
[12] R. Golub, C. Jewell, P. Ageron, W. Mampe, B. Heckel, and I. Kilvington, Z. Phys. B **51**, 187 (1983).
[13] A. I. Kilvington, R. Golub, W. Mampe, and P. Ageron, Phys. Lett. A **125**, 416 (1987).
[14] Y. Masuda, T. Kitagaki, K. Hatanaka, M. Higuchi, S. Ishimoto, Y. Kiyanagi, K. Morimoto, S. Muto, and M. Yoshimura, Phys. Rev. Lett. **89**, 284801 (2002).
[15] C. L. Morris *et al.*, Phys. Rev. Lett. **89**, 272501 (2002).
[16] A. Saunders *et al.*, Phys. Lett. B **593**, 55 (2004).
[17] F. Atchison *et al.*, Phys. Rev. C **71**, 054601 (2005).
[18] E. Gutsmiedl, A. Frei, A. R. Müller, S. Paul, M. Urban, H. Schober, C. Morkel, and T. Unruh, Nucl. Instrum. Methods **611**, 256 (2009).
[19] C. Y. Liu and A. Young, arXiv:nucl-th/0406004.
[20] J. Kreutz and H. J. Jodl, Phys. Rev. B **68**, 214303 (2003).
[21] S. A. Medvedev, J. Kreutz, and H. J. Jodl, J. Phys. Condens. Matter **15**, 7375 (2003).
[22] P. W. Stephens and C. F. Majkrzak, Phys. Rev. B **33**, 1 (1986).
[23] F. Dunstetter, O. Hardouin-Duparc, V. P. Plakhty, J. Schweizer, and A. Delapalme, Fiz. Nizk. Temp. **22**, 140 (1996) [Low Temp. Phys. **22**, 101 (1996)].
[24] F. J. Bermejo, A. de Bernabe, J. L. Martinez, M. L. Senent, G. J. Cuello, S. F. J. Cox, F. Dunstetter, and F. Trouw, J. Low Temp. Phys. **111**, 287 (1998).
[25] A. Serebrov *et al.*, Nucl. Instrum. Methods **440**, 658 (2000).
[26] F. Atchison *et al.*, Phys. Rev. Lett. **99**, 262502 (2007).
[27] G. C. DeFotis, Phys. Rev. B **23**, 4714 (1981).
[28] A. Jezowski, P. Stachowiak, V. V. Sumarokov, J. Mucha, and Y. A. Freiman, Phys. Rev. Lett. **71**, 97 (1993).
[29] M. Russina, F. Mezei, T. Kozlowski, P. Lewis, S. Penttila, J. Fuzi, E. David, and G. Messing, in *ICANS-XVI* (Forschungszentrum Jülich GmbH, Jülich, Germany, 2003), pp. 667–675.
[30] J. Fuzi, E. David, T. Kozlowski, P. Lewis, G. Messing, F. Mezei, S. Perittila, L. Rosta, M. Russina, and G. Torok, Phys. Condens. Matter **385**, 1315 (2006).
[31] S. Penttila and A. S. Bacci (private communication).
[32] P. N. Seo, J. D. Bowman, M. Gericke, G. Greene, J. Long, G. S. Mitchell, S. I. Penttila, and W. S. Wilburn, Nucl. Instrum. Methods **517**, 285 (2004).
[33] M. Ooi, T. Ino, G. Muhrer, E. J. Pitcher, G. J. Russell, P. D. Ferguson, E. B. Iverson, D. Freeman, and Y. Kiyanagi, Nucl. Instrum. Methods **566**, 699 (2006).
[34] W.-D. Seiffert, Europaische atomgemeinschaft Euratom, 1970 (unpublished).
[35] V. G. Manzhelii, A. Prokhvatilov, V. Gavrilko, and A. Isakina, *Structure and Thermodynamic Properties of Cryocrystals: Handbook* (Begell House, New York, 1998).
[36] R. W. Pattie *et al.*, Phys. Rev. Lett. **102**, 012301 (2009).
[37] C.-Y. Liu, S. K. Lamoreaux, A. Saunders, D. Smith, and A. R. Young, Nucl. Instrum. Methods **508**, 257 (2003).

[38] C. L. Morris *et al.*, Nucl. Instrum. Methods **599**, 248 (2009).
[39] A. Steuwer, J. R. Santisteban, P. J. Withers, L. Edwards, and M. E. Fitzpatrick, J. Appl. Crystallogr. **36**, 1159 (2003).
[40] F. Atchison, T. Brys, M. Daum, P. Fierlinger, A. Fomin, R. Henneck, K. Kirch, M. Kuzniak, and A. Pichlmaier, Nucl. Instrum. Methods **552**, 513 (2005).
[41] MCNP5 Monte Carlo N–Particle Transport Code System Including MCNP5 1.51 and MCNPX 2.6.0 and Data Libraries, RSICC CODE PACKAGE CCC-740, 2008.
[42] G. Zsigmond, K. Lieutenant, S. Manoshin, H. N. Bordallo, J. D. M. Champion, J. Peters, J. M. Carpenter, and F. Mezei, Nucl. Instrum. Methods **529**, 218 (2004).
[43] C. Y. Liu, A. R. Young, and S. K. Lamoreaux, Phys. Rev. B **62**, R3581 (2000).
[44] C. Y. Liu, A. R. Young, C. M. Lavelle, and D. Salvat, arXiv:1005.1016v1.
[45] T. Lauer, Ph.D. thesis, Universität Mainz, 2010.
[46] A. R. Müller, Ph.D. thesis, Technischen Universität München, 2008.